Available online at www.sciencedirect.com
ScienceDirect
International Journal of Heat and Fluid Flow 27 (2006) 980–993
International Journal of HEAT AND FLUID FLOW
www.elsevier.com/locate/ijhff

Some features of a turbulent wing–body junction vortical flow

Semih M. Ölçmen [a,*], Roger L. Simpson [b]

[a] Aerospace Engineering and Mechanics Department, The University of Alabama, Tuscaloosa, AL 35487, United States
[b] Aerospace and Ocean Engineering Department, Virginia Tech, Blacksburg, VA 24061, United States

Received 25 October 2005; received in revised form 26 January 2006; accepted 3 February 2006
Available online 11 April 2006

Abstract

Laser-Doppler velocimeter measurements of a wing/body junction flow field made within a plane to the side of the wing/wall junction and perpendicular both to a 3:2 elliptical nose—NACA 0020 tail wing, and a flat wall are presented. Reynolds number of the approach boundary layer was, $Re_\theta = 5940$, and free-stream air velocity was, $U_{ref} = 27.5$ m/s. A large vortical structure residing in the outer region redirects the low-turbulence free-stream flow to the vicinity of the wing/wall junction, resulting in thin boundary layers with velocity magnitudes higher than free-stream flow. Lateral pressure gradients result in a three-dimensional separation on the uplifting side of the vortex. Additionally, a high vorticity vortical structure with opposite sense to the outer-layer vortex forms beneath the outer-layer vortex. Normal and shear stresses increase to attain values an order of magnitude larger compared to values measured in a three-dimensional boundary layer just outside the junction vortex. Bimodal histograms of the w fluctuating velocity occur under the outer-layer vortex near the wall due to the time-dependent nature of the horseshoe vortex. In such a flow the shear-stress angle (SSA) highly lags the flow-gradient angle (FGA), and the turbulence diffusion is highly altered due to presence of vortical structures.
© 2006 Elsevier Inc. All rights reserved.

Keywords: Turbulence; Wing/body junction flow; Three-dimensional boundary layer; Laser-Doppler velocimeter

1. Introduction

1.1. Flowfield description—previous experimental observations

Wing-body junction separated vortical flows have been the subject of many past studies. Reviews by Simpson (1996, 2001) give the key features of the nose-region flow, which are summarized here. A "horseshoe vortex" forms at the nose of the wing at a junction because the spanwise vorticity in the approach boundary layer rolls up and is stretched around the body (Fig. 1). A "closed" time-averaged separation line starts from the 3D stagnation point and is located around each side of the wing. Time-averaged backflow is present between this stagnation point and the nose. Devenport and Simpson (1987, 1990a) show that a line of low shear also is located between this closed separation line and the wing nose and merges with the closed separation line at the side of the model.

For a sufficiently blunt nose, such as the 3:2-elliptic-nose/NACA 0020-tail wing (Rood body) in the present work, the flow in front of the nose shows aperiodic low-frequency self-induced switching between velocity states that produce double-peaked (bimodal) fluctuating velocity probability histograms with very large Reynolds stress values, as compared to the approaching boundary layer (Devenport and Simpson, 1990a). Bimodal high surface pressure fluctuation levels (Ölçmen and Simpson, 1994) and high heat transfer rates (Lewis et al., 1994) occur in this region. The approach flow Reynolds number is not a dominant factor for the existence of the bimodal behavior. The wing shape is the major factor because it largely determines the pressure gradients in front of and around the wing and the rate of stretching of the "horseshoe vortex" around the wing. The 3-velocity-component LDV wind tunnel data of Devenport and Simpson (1990b, 1992) show

* Corresponding author. Fax: +1 205 348 7240.
E-mail addresses: solcmen@coe.eng.ua.edu (S.M. Ölçmen), simpson@aoe.vt.edu (R.L. Simpson).

0142-727X/$ - see front matter © 2006 Elsevier Inc. All rights reserved.
doi:10.1016/j.ijheatfluidflow.2006.02.019

Nomenclature

C_p	static pressure coefficient
$(\partial C_p/\partial s)$	static pressure coefficient gradient
q^2	$q^2 = u^2 + v^2 + w^2$
TKE	turbulent kinetic energy, $\frac{1}{2}\overline{q^2}$
U, V, W	mean velocity components
u, v, w	fluctuating velocity components
$U^+ = U/u_\tau$	non-dimensional mean velocity
$u_\tau = \sqrt{\tau_w/\rho}$	skin-friction velocity
x_{TC}, y, z_{TC}	tunnel coordinates
$x_{22.4}, y, z_{22.4}$	coordinates in which x and z axes are oriented at 22.4° with respect to the tunnel coordinates
$y^+ = yu_\tau/\nu$	wall-law variable
δ	boundary layer thickness
$\theta = \int_0^\infty \left(1 - \frac{U}{U_e}\right)\frac{U}{U_e}\,dy$	momentum thickness
σ	standard deviation
τ_w	wall shear stress

that the bimodal structure exists for the velocity y components perpendicular to the horseshoe vortex core around the front of the wing where the flow is accelerating and the elliptically-shaped vortex is being stretched.

The flow visualization water tunnel studies of Kim et al. (1991) and Khan et al. (1995) for this wing shape describe the time development of the motion. While the "horseshoe vortex" nearest the wing nose is being stretched, newer younger vortices are formed downstream of the 3D separation. The younger vortices grow with time while the oldest vortex is being reduced in size by stretching. Eventually one or more of these new vortices merge with what is left of the oldest one to form another "old" large-scale vortex nearest the nose. The process is then repeated, although the process is never periodic and appears to be Markovian (Ölçmen et al., 1991).

Fleming et al. (1993) examined available data sets for Rood wing/body junction flows from several different research groups (McMahon et al., 1982, 1987) over a range of approach momentum thickness Reynolds numbers, Re_θ and boundary layer to wing thickness ratios δ/t. The product of Reynolds number, Re_t based on the maximum thickness, t, and Re_θ, or Fleming's approach flow "momentum deficit factor" MDF, correlated observed effects on the flow in the downstream adverse pressure gradient region around the wing and in the wake. As MDF increases, streamwise velocity distortions decrease, secondary flow patterns are more elliptic, the vortex core and the vorticity are closer to the wall, the spanwise spacing of the legs of the vortices increase in the wake, and the core vorticity and helicity levels increase when non-dimensionalized on δ and U_{ref}. Many flow features scale on maximum thickness, t, in all directions, since the pressure gradient distribution is largely governed by the wing shape and thickness.

1.2. Results from previous computational studies

This flow field has been used as a computational test case, e.g. Sung and Yang (1988), Bonnin et al. (1996), Parneix et al. (1998), Deng and Visonneau (1999) and Apsley and Leschziner (2001). Rizzi and Vos (1998) describe a method of establishing credibility in CFD codes.

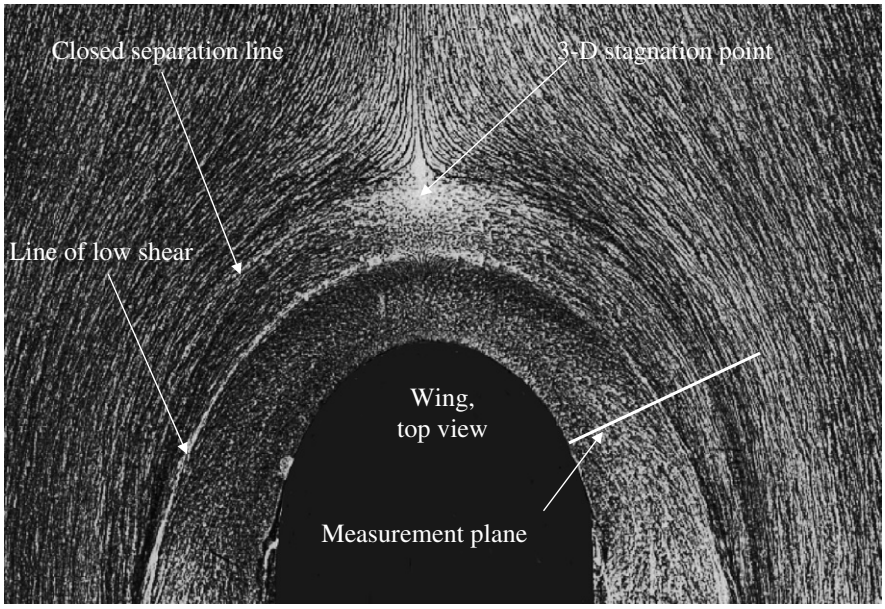

Fig. 1a. Oil flow visualization obtained on the wall. Line denotes the measurement plane.

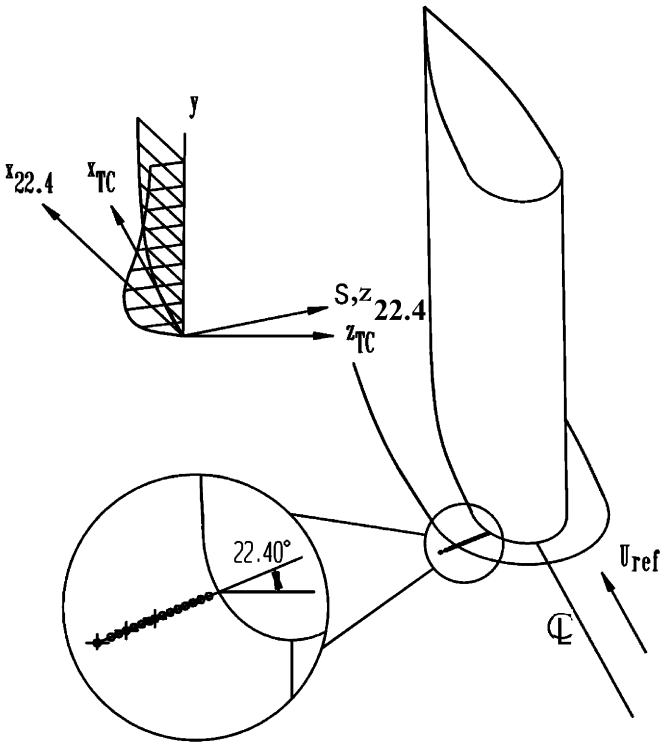

Fig. 1b. Measurement locations and definitions of coordinate systems. "s" direction same as "$z_{22.4}$".

Sung and Yang (1988) used the Baldwin-Lomax zero-equation turbulence model to calculate the flow field and compared the three-mean velocity components to the data obtained from different groups including the Virginia Tech, Gerogia Tech, and David Taylor Research Center. Their results show that the size and strength of the vortical structures near the nose and at the side of the wing are underpredicted by this approach, due to the isotropic eddy-viscosity model used in a highly three-dimensional flow.

Bonnin et al. (1996) on the other hand compared the results of seven different computer codes from seven different groups to the data of Fleming et al. (1993) and Devenport and Simpson (1990a,b). While six of the computer codes used versions of k–ε model, one used a Reynolds stress model (RSM). Five of these models used wall-functions and the other two used two-layer approach. Results showed that all the codes underpredicted the strength and size of the vortex around the wing and near the nose region, underpredicted the TKE values within the separation vortex that forms near the nose region, and overpredicted the TKE values near the stagnation region. Specifically the use of the wall functions was considered as the main reason for the differences since the flow field includes regions with $\partial U/\partial y = 0$, where any present law-of-the-wall would not hold. Additional reasons were attributed to the modeling of terms in Reynolds-stress models indicating the need for further data in such complex flows.

Parneix et al. (1998) calculated the flow field using a standard k–ε model, modified for near-wall turbulence anisotropy and non-local pressure-strain effects, while maintaining a linear eddy-viscosity assumption (named as the V2F model). The calculations were compared with the experimental data (Ölçmen and Simpson, 1997 and Devenport and Simpson, 1990a,b), reasonably well, especially at the locations along the side of the wing.

Deng and Visonneau (1999) used a new Reynolds-stress model ($R_{ij} - \omega$), which could be considered as the extension of Wilcox's k–ω model to Reynolds-stress modeling. They used the data of Devenport and Simpson (1990a,b), Fleming et al. (1993) and Ölçmen and Simpson (1995a,b). Their results showed that compared to Chen–Patel standard k–ε model their model predictions were in better agreement with the data although the data overestimated the U mean velocity component and underestimated the W mean velocity component, and only approximately captured the variation of the Reynolds stresses.

Study made by Apsley and Leschziner (2001) using Devenport and Simpson (1990a,b) and Fleming et al. (1993) data summarizes the research findings of turbulence-model validation group formed by UMIST, Loughborough University, BAE Systems, Aircraft Research Association, Rolls-Royce and DERA. In this study the group used 12 different turbulence closure models. Three classes of turbulence models were investigated by the group: linear (or 'isotropic') eddy-viscosity models, non-linear (or 'anisotropic') eddy-viscosity formulations (NLEVMs), and differential stress ('second-moment closure') models (DSMs). Their findings showed that while the second-moment closure schemes predict the flow better than the other models the size and shape of the vortex in the nose region is underestimated and the turbulence quantities such as the TKE is only approximately estimated by these models.

1.3. Present experimental details, motivation and paper outline

Conditions of the present flow field are well documented (Simpson, 1996). The approach flow conditions, surface oil flows, and wall-static pressure distribution were previously presented (Ölçmen, 1990; Ölçmen and Simpson, 1995a and Simpson, 2001). Devenport and Simpson (1990b) and Ölçmen (1990), Ölçmen and Simpson (1995a, 1996a,b,c,d,e) present data in the 3D boundary layer outside of the horseshoe vortex. Devenport and Simpson (1990b, 1992) and Fleming et al. (1993) made measurements of the two components of the mean flow and three components of the Reynolds' stress tensor at several planes along the side and in the wake of the wing. Ailinger (1990) measured the surface skin-friction at the locations using oil-film interferometry.

In contrast to the previous studies, more accurate fine-spatial-resolution near wall information is presented not only of the mean flow and Reynolds stresses, but also of the triple products which are presented for the first time for this type of flow. Fig. 1 shows the measurement loca-

tions around the side of the nose and the coordinate axes used in the present study. All the data, unless otherwise specified, are presented in a coordinate system where $x_{22.4}$ is perpendicular to the plane of measurements, "s" is in the plane of the measurements with positive axis towards the wing, and y-axis is perpendicular to the wall. The origin is at the junction of the wing and the wall.

The flow study undertaken here provides a unique, well documented data set for the developers of advanced turbulence models to test their model equations. It is well known that the isotropic eddy-viscosity models can not predict three-dimensional turbulent flow well (Launder and Sandham, 2002) and data including the third order moments are required for testing and developing models such as the non-linear eddy-viscosity models or the Reynolds-stress models. The data presented provide detailed data about a three-dimensional turbulent boundary layer to aid understanding the flow-physics of such flows.

The five-component laser-Doppler velocimeter used for the measurements in the Virginia Tech, AOE Department, boundary layer wind tunnel and the data acquisition and reduction techniques were previously discussed (Ölçmen and Simpson, 1995a,b) and are described here very briefly. The effective probe volume had a diameter of 30 μm. The probe volume could traverse as close as 50 μm to the wall and the wall location could be determined with an uncertainty of ±10 μm. The coincident three velocity components in the optical coordinate system were transformed to the $x_{22.4}$, y, s coordinate systems. The noise on the skirts of the histograms of the velocity was removed after fitting a parabola to the logarithm of the histograms. The inverse-velocity-magnitude bias-corrected histograms calculated using the cleaned data were used to extract the mean velocity and higher order terms. Table 1 gives the flow characteristics at the 15 measurement stations along s. There were 31 logarithmically spaced y measurement locations per station. Table 2 gives 21:1 uncertainties calculated using two separate data sets measured at one of the measurement locations and using Chauvenet's criterion (Holman, 2000) to define the uncertainty. The skin-friction was determined by a curve fit to the viscous sublayer velocity profile, as discussed by Ölçmen and Simpson (1995a). Contour plots were formed using Tecplot.

In the following sections mean velocity, Reynolds stress, and selected triple product contour plots are used to describe the flow features, including the bimodal nature of the fluctuating velocity probability density distributions. In each contour plot the secondary-flow streamlines obtained using the V and the W components of the mean velocity are also plotted. Secondary-flow streamlines serve the purpose of a template to show the relatively important locations of the flow quantities of interest to each other. Some derived quantities such as the flow angle, flow-gradient angle, the shear-stress angle and the eddy-viscosity ratio are also discussed. Remaining quantities can be found in the report by Ölçmen and Simpson (1996d).

The results are presented using a logarithmic scale on the ordinate to emphasize and show the near-wall variation of the quantities of interest. Both in the abscissa and the ordinate the maximum thickness of the wing, t, is used as the length scale since the flow characteristics depend on the thickness of the wing rather than the approach boundary layer thickness. The conventional wall units, y^+, are not used in the presentation since the wall-skin-friction values change from station to station. However, for comparison purposes a distance, $y = 72.6$ μm away from the wall corresponds to the $\log_{10}(y/t) = -3$, and corresponds to $y^+ = 5$ using $U_\tau = 1.15$ m/s and $v = 1.67\text{e}{-05}$ m^2/s, which are the parameters for the most outboard station.

Table 1
Laser-Doppler velocimeter locations and flow parameters

Stations	X (mm)	Z (cm)	U_e (m/s)	U_τ (m/s)	β_w (degree) in 22.4°	β_{FS} (degree) in 22.4°	δ (mm)	s/t	$(\partial C_p/\partial x)$(1/m) in 22.4°	$(\partial C_p/\partial z)$ (1/m) in 22.4°
Station 5	6.60	−7.47	29.54	1.15	2.7	14.7	40	−0.6774	−5.551	−3.471
A	8.79	−6.94	29.74	1.094	2.276	13.12	39.6	−0.589	−6.402	−5.195
B	9.98	−6.64	29.94	1.002	−0.647	12.53	39.9	−0.545	−7.025	−5.994
C	11.2	−6.35	30.2	1.048	−1.195	12.02	39.3	−0.501	−7.701	−6.671
D	12.42	−6.06	30.45	1.093	−2.409	11.41	39.2	−0.456	−8.249	−7.983
E	13.61	−5.77	30.65	1.132	−3.184	10.88	40.3	−0.412	−8.782	−9.488
TB	14.83	−5.47	31.82	1.163	−3.858	9.83	39.7	−0.368	−9.754	−10.455
TC	15.7	−5.26	32.27	1.188	−7.074	9.29	40.9	−0.336	−10.884	−9.813
R	16.92	−4.97	32.58	1.297	−15.583	8.21	39.2	−0.291	−11.654	−10.579
S	18.11	−4.67	33.15	1.362	−20.741	7.09	40.3	−0.247	−12.193	−5.293
T	19.33	−4.38	33.72	1.413	−18.914	5.77	38.9	−0.203	−14.54	−4.502
U	20.55	−4.09	34.85	1.320	−13.539	4.24	39.3	−0.159	−15.129	−5.093
V	21.74	−3.79	36.29	1.454	−10.943	2.82	38.4	−0.114	−13.134	−8.909
W	22.96	−3.50	37.56	1.656	−10.888	1.02	28.6	−0.070	1.456	−0.949
X	24.26	−3.18	40.42	1.917	10.752	−0.17	20.6	−0.023	1.472	−0.933

Station names in the first column start with the most outboard station. Maximum thickness of the wing (t) = 7.17 cm, Nominal reference velocity (U_{ref}) = 27.5 m/s, Reynolds number based on momentum thickness at 0.75 chord upstream of the wing on the tunnel centerline (Re_θ) = 5940. Wing chord length = 30.48 cm. β_{FS} flow angle at the boundary layer edge, β_{WC} wall-stress direction.

Table 2
21:1 odds $\pm 2\sigma$ uncertainties of mean velocities, Reynolds stresses and triple products

Term	Uncertainty $\times 10^{-03}$	Term	Uncertainty $\times 10^{-06}$
U/U_{ref}	5.64	$\overline{u^2v}/U_{ref}^3$	4.54
V/U_{ref}	1.25	$\overline{u^2w}/U_{ref}^3$	7.97
W/U_{ref}	3.7	$\overline{v^2w}/U_{ref}^3$	2.82
$\overline{u^2}/U_{ref}^2$	0.09	$\overline{uv^2}/U_{ref}^3$	3.04
$\overline{v^2}/U_{ref}^2$	0.0581	$\overline{uw^2}/U_{ref}^3$	9.13
$\overline{w^2}/U_{ref}^2$	0.01017	$\overline{vw^2}/U_{ref}^3$	2.93
$\overline{uv}/U_{ref}^2$	0.0363	$\overline{uvw}/U_{ref}^3$	2.77
$\overline{uw}/U_{ref}^2$	0.0537	$\overline{u^3}/U_{ref}^3$	14.06
$\overline{vw}/U_{ref}^2$	0.0276	$\overline{v^3}/U_{ref}^3$	2.38
		$\overline{w^3}/U_{ref}^3$	23.47

2. Mean flow field

As mentioned before, the non-periodic vortical flow developing at the nose region and subsequent stretching and reorientation of this vortical flow along the wing contour results in a large rotational region, which shapes the structure of the entire wing–wall junction flow. Mean velocity contours and the secondary streamlines in the measurement plane (Figs. 2a, 2b, and 2c) indicate three flow regions of interest; (i) a large clockwise vortical structure located in the outer region with its core at $\log_{10}(y/t) = -1.1$ and $s/t = -0.32$, (ii) a three-dimensional separation region around $s/t = -0.58$, below $\log_{10}(y/t) = -2.5$, and, (iii) a counter-clockwise vortical flow region near the wing wall junction below $\log_{10}(y/t) = -1.7$. The mean velocity contours obtained within the measurement plane are discussed below.

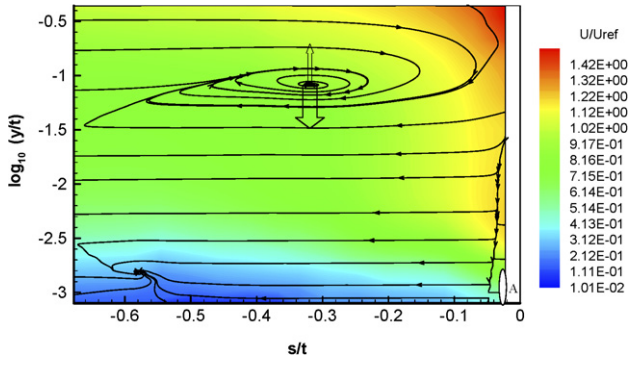

Fig. 2a. U/U_{ref} velocity magnitude contours and secondary flow streamlines. Region A shows the region, where the vorticity vector spanwise component shows a peak, $-\frac{\omega_z t}{U_{ref}} = 464$. Empty arrows denote the intermittent movement of the vortical structure.

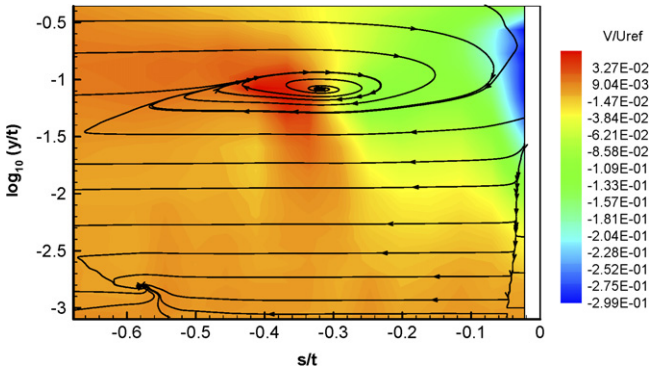

Fig. 2b. V/U_{ref} velocity magnitude contours and secondary flow streamlines.

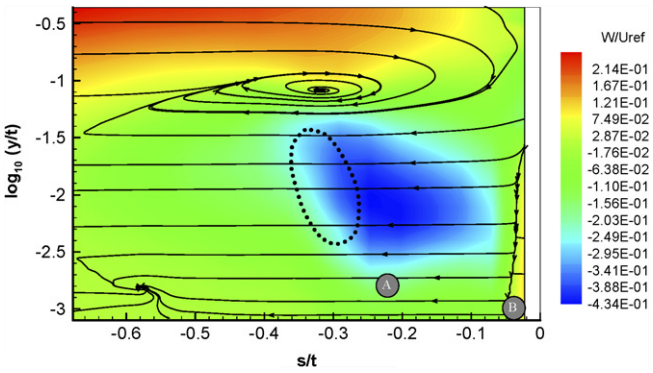

Fig. 2c. W/U_{ref} velocity magnitude contours and secondary flow streamlines. Region A shows the region, where vorticity vector streamwise component shows a negative peak, $\frac{\omega_x t}{U_{ref}} = -108$, and region B shows the region for the positive peak, $\frac{\omega_x t}{U_{ref}} = 58$. Dashed lines surround the region, where w fluctuating velocity component show bimodal histograms.

U mean velocity contours (Fig. 2a) show that the acceleration of the flow around the wing and the high speed free-stream fluid directed towards the wing/wall junction by the outer-layer vortex results in U velocity components higher than the free-stream approach velocity in the zone between the vortex core and the wing. High velocities redirected to the wing/wall junction results in positive $\partial U/\partial s$ gradients everywhere except near the three-dimensional separation region around $s/t = -0.55$, and it also results in $\partial U/\partial y$ gradients which are approximately zero to the lower right of the vortex core between the vortex core and the wing, where a law-of-the-wall for the U component would not hold. Near the wall ($\log_{10}(y/t) \approx -2$), $\partial U/\partial y$ gradients also increase towards the wing indicating increased wall-shear stress as the wing is approached.

The free-stream fluid directed towards the wing/wall junction also results in high negative V velocity components closer to the wing in the region between the large outer-layer vortex and the wing (Fig. 2b). Positive and small magnitude V velocities are observed on the uplifting side of the vortex. The rolling motion within the measurement plane at locations closer to the wall redirects the flow away from the wing parallel to the floor.

In this flow, high speed negative W velocity components faster than the outer layer positive W free-stream velocity component are observed between the outer-layer vortex and the wall (Fig. 2c). The lateral pressure gradient $\partial C_p/\partial s$ values obtained on the wall in the plane of the measurements are tabulated in Table 1 and show that the wall-static pressure is decreasing in the s direction. Although the high speed W velocity energizes the near wall flow under

the vortex and produces large $\overline{w^2}$, the near wall low momentum fluid affected by the lateral pressure gradients separates at $s/t = -0.55$, as shown by the convergence of the secondary streamlines. Near the wing and the wall intersection, the W velocity component values change sign and become positive resulting in a counter-clockwise corner vortex, which has locally high negative spanwise vorticity $\omega_s t/U_{\text{ref}}$ (Fig. 2a) and positive streamwise vorticity, $\omega_x t/U_{\text{ref}}$ (Fig. 2c) levels. Spanwise vorticity calculated using $\omega_s = -\partial U/\partial y$, indicate that both the $\partial U/\partial y$ gradient and thus the wall-shear stress values are large in this region. Positive streamwise vorticity calculated using $\omega_x = \partial W/\partial y$ indicates that the lateral flow in the positive s direction is increasing away from the wall in this region, consistent with the W mean velocity results. Positive streamwise $\omega_x t/U_{\text{ref}}$ (Fig. 2c) vorticity levels are observed above $\log_{10}(y/t) = -2$ $(y^+ = 50)$ throughout the measurement plane.

3. Structure of the flow in selected regions

In this section, the second and higher order velocity products are discussed within the three-dimensional separation, the large outer region vortex, and near the wing and wall intersection region, which show different vortical flow structures. Additionally, these flow quantities are also discussed for a region under the large outer-layer vortex near the wall, where the velocity components in that region show a bimodal velocity structure that produces large turbulence quantities. To aid the discussion here, contour plots of the kinematic Reynolds stresses are shown in Figs. 3 and 4. Fig. 5 shows a summary map of locations for some key conditions for the various Reynolds stresses and some derived quantities. Figs. 6a, 6b and 6c show some triple product contour plots. Fig. 7 is a summary map of locations for key conditions for triple products. Discussion of many other quantities is contained in the report by Ölçmen and Simpson (1996d).

3.1. Three-dimensional separation region

Since the measurement plane is about perpendicular to the separation line (Fig. 1), $W = 0$ (Fig. 2c) in this plane

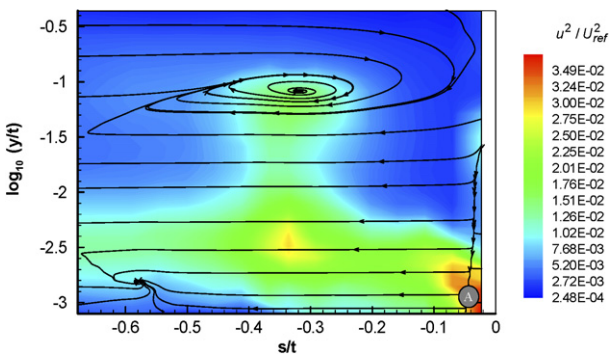

Fig. 3a. $\overline{u^2}/U_{\text{ref}}^2$ normal stress contours and secondary-flow streamlines.

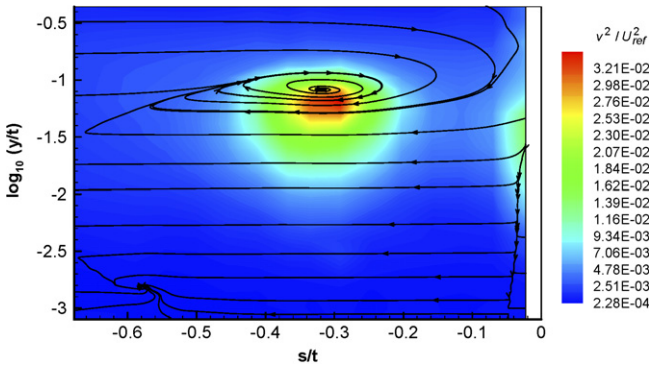

Fig. 3b. $\overline{v^2}/U_{\text{ref}}^2$ normal stress contours and secondary-flow streamlines.

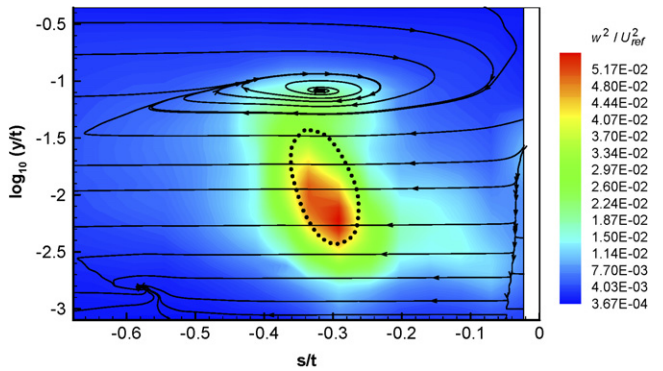

Fig. 3c. $\overline{w^2}/U_{\text{ref}}^2$ normal stress contours and secondary-flow streamlines. Dashed lines surround the region, where w fluctuating velocity component show bimodal histograms.

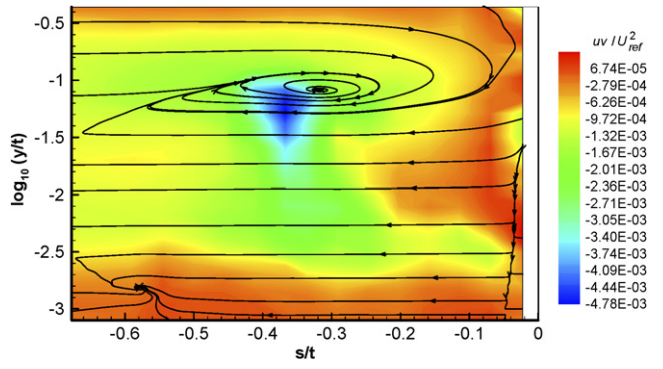

Fig. 4a. $\overline{uv}/U_{\text{ref}}^2$ shear stress contours and secondary-flow streamlines.

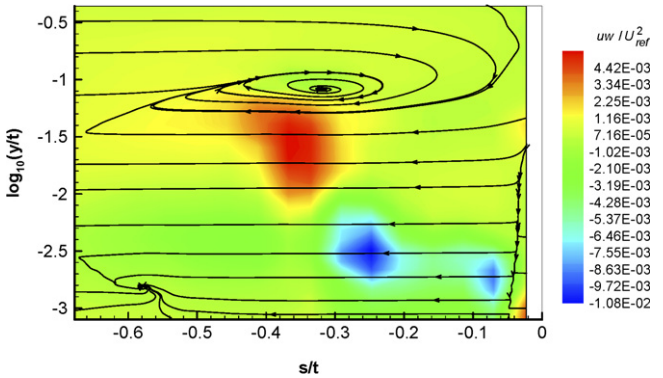

Fig. 4b. $\overline{uw}/U_{\text{ref}}^2$ shear stress contours and secondary-flow streamlines.

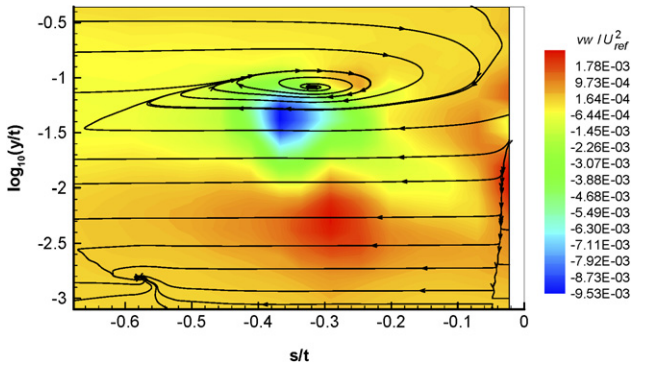

Fig. 4c. $\overline{vw}/U_{ref}^2$ shear stress contours and secondary-flow streamlines.

shows the location of a 3D separation. Mean secondary-flow streamlines merge in the plane of the measurements away from the wall, but still in the viscous sublayer ($\log_{10}(y/t) \approx -2.8$, $y^+ \approx 7$), and indicate separation of the flow from the floor around $s/t \approx -0.55$, or about where the oil-flow streamlines indicate separation (Fig. 1). The mean streamwise vorticity of this region is opposite to that of the large outer-layer vortex. As noticed in other 3D separations (Wetzel et al., 1998), the mean velocity magnitude is locally low around the separation region with an observed near minimum in skin-friction magnitude (Table 1).

The peak $\overline{u^2}$ normal stresses occurring across the separation ($-0.59 < -s/t < -0.50$) at $\log_{10}(y/t) \approx -2.5$ ($y^+ = 15$) (Fig. 3a) and the peak $\overline{uv}$ velocity product at $\log_{10}(y/t) \approx -2.17$ ($y^+ = 30$) (Fig. 4a) show a local decrease on the updraft side of this rotational separation. Within the separation region the average skin-friction velocity is, $u_\tau = 1.028$ m/s, and any second and third order products non-dimensionalized with the u_τ can be expressed as non-dimensionalized with the $U_{ref} = 27.5$ m/s using the relations $\overline{()}/U_{ref}^2 = \overline{()}/u_\tau^2 \times 1.397\text{E}-3$ and $\overline{()}/U_{ref}^3 = \overline{()}/u_\tau^3 \times 5.224\text{E}-5$, respectively. The spanwise peak normal stress varies between $1.3 < \overline{w^2}/u_\tau^2 < 2.3 (1.8\text{E}-3 < \overline{w^2}/U_{ref}^2 < 3.2\text{E}-03)$ across the separation at $y^+ \approx 10$ ($\log_{10}(y/$

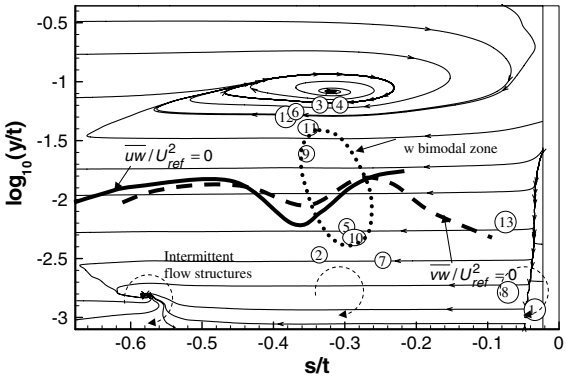

Zones		
1	$\overline{u^2}/U_{ref}^2$ =0.035, maximum	
2	$\overline{u^2}/U_{ref}^2$ =0.028, local peak	
3	$\overline{u^2}/U_{ref}^2$ =0.016, local peak	TKE/U_{ref}^2 =0.0354, maximum
4	$\overline{v^2}/U_{ref}^2$ =0.032, maximum	
5	$\overline{w^2}/U_{ref}^2$ =0.052, maximum	TKE/U_{ref}^2 =0.0354, maximum
6	$-\overline{uv}/U_{ref}^2$ =0.00449, maximum	
7	$-\overline{uw}/U_{ref}^2$ =0.0099, maximum	
8	$-\overline{uw}/U_{ref}^2$ =0.0089, local peak	
9	$\overline{uw}/U_{ref}^2$ =0.0045, maximum	
10	$\overline{vw}/U_{ref}^2$ =0.00183, maximum	
11	$-\overline{vw}/U_{ref}^2$ =0.00885, maximum	
12	A_1=0.18, maximum	
13	A_1=0.0012, minimum	

Fig. 5. Summary map locations of peak second order product quantities.

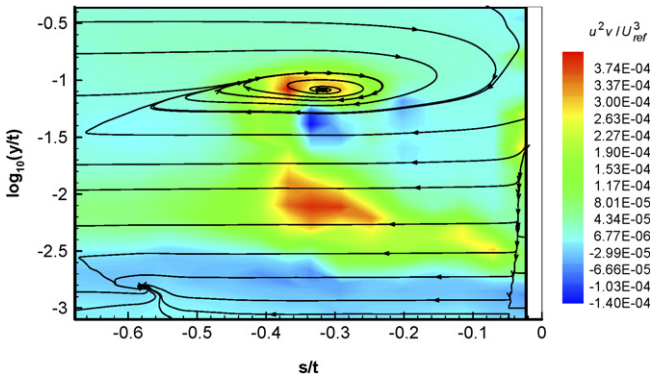

Fig. 6a. $\overline{u^2v}/U^3_{ref}$ Summary map locations of peak second-order product quantities.

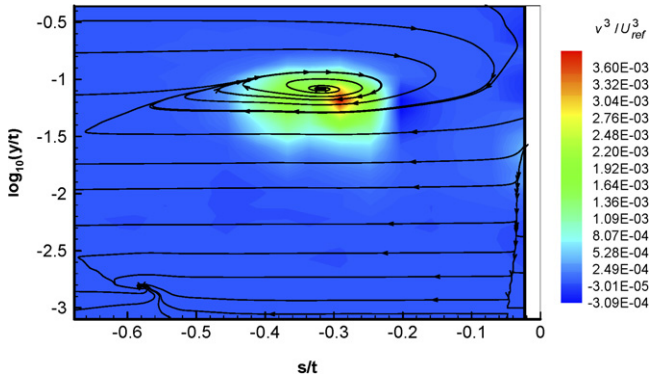

Fig. 6b. $\overline{v^3}/U^3_{ref}$ Summary map locations of peak second-order product quantities.

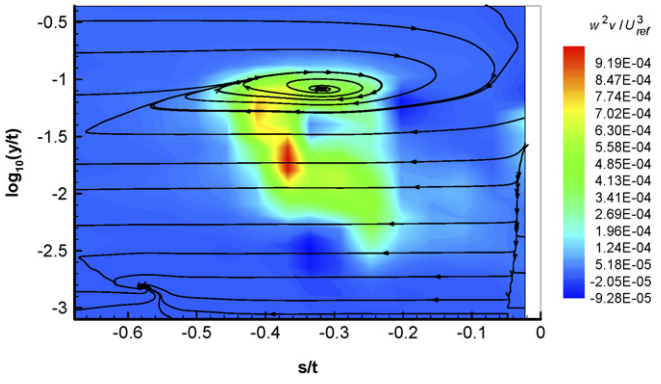

Fig. 6c. $\overline{vw^2}/U^3_{ref}$ Summary map locations of peak second order product quantities.

$t) \approx -2.64$, ~144 μm from the wall); farther from the wall this normal stress increases with s due to flow structures affecting the bimodal w flow region (Fig. 3c). The near-wall $\overline{v^2}$ is also not affected much by the separation, but farther away from the wall the increase in $\overline{v^2}$ values toward the wing seems to be due to the effect of the large scale outer vortex (Fig. 3b). The $\overline{vw}/u_\tau^2$ maximum value, located near $\log_{10}(y/t) \approx -2.25$ or $y^+ \approx 25$, varies between $0.18 < \overline{vw}/u_\tau^2 < 0.3 (2.5\text{E}-4 < \overline{vw}/U^2_{ref} < 4.2\text{E}-4)$ (Fig. 4c) across the separation. The $-\overline{uw}/u_\tau^2$ maximum value, located near $y^+ \approx 20 (\log_{10}(y/t) \approx -2.34)$, also increases across the separation, and varies between $0.87 < -\overline{uw}/u_\tau^2 < 1.7$, $(1.2\text{E}-3 < -\overline{uw}/U^2_{ref} < 2.38\text{E}-03)$ (Fig. 4b). The u and $-w$ and the v and w fluctuations are more correlated, i.e. produce more stresses, within the rotational separation region as compared to a station outside the separation ($s/t = -0.677$).

The triple products provide some insights to the motions that occur around the separation. These values are relatively small compared to values in the large vortex and bimodal w regions and are not observable in Figs. 6 and 7. Near the wall ($y^+ < 20$) $\overline{vw^2}$, $\overline{v^2w}$, $\overline{uv^2}$, and $\overline{v^3}$ triple products are about zero and vary about the same as at a station outside the separation region ($s/t = -0.667$). They are only weakly affected by the separation.

Near the wall ($y^+ \approx 10$) sweep motions ($u > 0, v < 0, w < 0$) are seen as the dominant motions. Intermittent, high-speed flow structures initiating from the outer layer result in intermittent high fluctuating velocities within this region and shape the structure of the triple products. The near-wall maxima of $-\overline{u^2v}/u_\tau^3 \approx 0.8 (-\overline{u^2v}/U^3_{ref} \approx 4.18\text{E}-5)$, and $\overline{uvw}/u_\tau^3 \approx 0.2 (\overline{uvw}/U^3_{ref} \approx 1.0\text{E}-5)$ are located around $y^+ \approx 10 (\log_{10}(y/t) \approx -2.64)$. The near-wall maxima of $\overline{u^3}/u_\tau^3$, $\overline{uw^2}/u_\tau^3$, and $-\overline{u^2w}/u_\tau^3$ located around $y^+ \approx 10$, increase with s through the separation with $8 < \overline{u^3}/u_\tau^3 < 12$, $1.8 < \overline{uw^2}/u_\tau^3 < 3.4$ and $1.2 < -\overline{u^2w}/u_\tau^3 < 2.2$. The peak $-\overline{w^3}/u_\tau^3$ obtained at $y^+ \approx 20$ also vary between $1.7 < -\overline{w^3}/u_\tau^3 < 4$ across the separation zone. Additionally the magnitude of $\overline{w^3}/u_\tau^3$ first increases away from the wall from a zero value to a peak value at $y^+ = 20$ and next decreases up to about $y^+ = 40$ indicating the high velocity negative w fluctuations occur less away from the wall.

Above the separation region, at around $y^+ = 30$ the dominant motions are the ejection motions ($u < 0, v > 0, w > 0$). High-speed flow initiating from the outer layer and resulting in sweep motions near the wall causes the low speed momentum near wall flow to rise away from the wall resulting in ejection motions. The local maxima of opposite signs of the near wall flow occur around $y^+ \approx 30$ and vary above the separation with increasing s; $1 < \overline{u^2v}/u_\tau^3 < 2$; $5 < -\overline{u^3}/u_\tau^3 < 8$; $0.8 < \overline{u^2w}/u_\tau^3 < 1.2$, $0.3 < \overline{-uvw}/u_\tau^3 < 0.35$.

The signs of the triple products involving the w fluctuating velocity indicate that the sweep motions occur with negative velocity fluctuations with a peak value around $y^+ = 10$ and the ejection motions occur together with positive w velocity fluctuations. This indicates that intermittent clockwise vortical motions may be aiding in shaping the triple product structure within the separation region, which has predominant counter-clockwise separation vortex.

The sweep motions also produce larger triple product magnitude values on the updraft side of the separation than on the down draft side, since U and $\overline{u^2}$ are smaller for a given y on the updraft side. Ejection motions also seem more dominant above the y locations where $\overline{vq^2} = 0$ and $\overline{u^3} = 0$, as shown in Fig. 7.

3.2. Flow surrounding the large vortex core

The region discussed here is limited to regions surrounding the large outer-layer vortex core between $-0.56 < s/t < -0.1$ and regions above ($\log_{10}(y/t) \approx -1.5$), to separate the discussion of the bimodal velocity region and the outer-layer vortex effects.

The secondary-flow streamlines indicate a rotating structure in the outer layer whose core is located at about $s/t = -0.32$ and $\log_{10}(y/t) \approx -1.1$, with the vorticity values that are small compared to the near-wall vorticity values. However, the circulation is large in this region since it covers a large area. The maximum V velocities with different signs (Fig. 2b) are observed on both sides of the vortex core and the W velocities (Fig. 2c) change sign through the vortex core. The W sign change occurs at increasing distances away from the wall proceeding towards the wing.

Local maxima of the $\overline{u^2}$ normal stress (Figs. 3a and 5) are located nearly under the vortex core. The dominant normal stress near the vortex core is $\overline{v^2}$ (Figs. 3b and 5) with values at least twice as large as nearby $\overline{u^2}$, and larger than the maximum $\overline{u^2}$ value which is near the wall. The $\overline{w^2}$ (Fig. 3c) and $\overline{v^2}$ (Fig. 3b) stresses decrease on both sides of the vortex core.

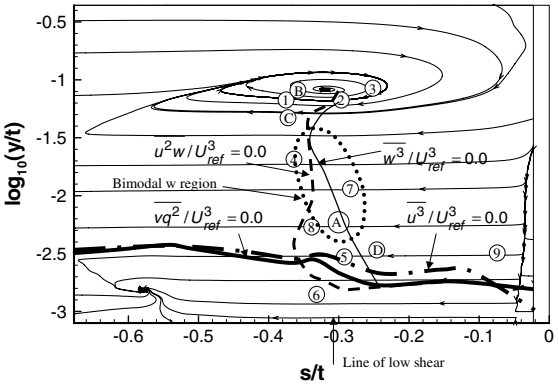

Zones		
A	TKE / U_{ref}^2 =0.035, peak	$\overline{u^2v} / U_{ref}^3$ =0.00038
B	$\overline{vq^2} / U_{ref}^3$ =0.054, local peak	$\overline{u^2v} / U_{ref}^3$ =0.00038
C	$\left[\left(\overline{uv^2}\right)^2 + \left(\overline{vw^2}\right)^2\right]^{1/2} / U_{ref}^3$ =0.00127, peak	$-\overline{uv^2} / U_{ref}^3$ =0.0004
D	$\overline{u^2w} / U_{ref}^3$ =0.0016, peak	$-\overline{uw^2} / U_{ref}^3$ =0.00117
1	$\overline{v^3} / U_{ref}^3$ =0.0017, local peak	$-\overline{v^2w} / U_{ref}^3$ =0.00088, $\overline{vq^2} / U_{ref}^3$ =0.06, peak
2	$\overline{v^3} / U_{ref}^3$ =0.0036, peak	$\overline{vq^2} / U_{ref}^3$ =0.06, peak
3	$-\overline{v^2w} / U_{ref}^3$ =0.00021, peak	
4	$-\overline{vw^2} / U_{ref}^3$ =0.0009, peak	
5	$\overline{uw^2} / U_{ref}^3$ =0.00116, peak	
6	$\overline{u^3} / U_{ref}^3$ =0.0016, peak	
7	$\overline{w^3} / U_{ref}^3$ =0.004, peak	
8	$-\overline{w^3} / U_{ref}^3$ =0.006, peak	
9	$-\overline{u^3} / U_{ref}^3$ =0.004, peak	

Fig. 7. Summary map of locations of peak triple product quantities.

Below the vortex core and towards the wing, U mean velocity profiles (Fig. 2a) show regions where $\partial U/\partial y$ is zero or even negative (between $\log_{10}(y/t) \approx -2$ to -1.25), which indicates that the production of $\overline{u^2}$ stress is small. In this same region the usually small $-\overline{uv}\frac{\partial V}{\partial y}$ production term for $-\overline{uv}$ becomes relatively important. Consequently, the peak $-\overline{uv}$ (3.5 times larger than at $s/t = -0.667$, the most outboard station) occurs away from these regions and is located under the large outer layer vortex away from the wing (Fig. 4a).

The $-\rho\overline{uv}$, $-\rho\overline{uw}$, $-\rho\overline{vw}$ are the apparent shear stresses that act on a fluid element to retard the element's rotation along the $+s$, $+y$, and $+x_{22.4}$ directions, respectively. Both on the uplifting and the downwash side of the outer-layer vortex $\overline{uw}$ kinematic stress is positive, and the positive peak observed under the vortex core is as high as the $-\overline{uv}$ kinematic stress. The positive $\overline{uw}$ sign throughout the region indicates that the flow has rotational motions along the $-y$ axis. The $-\overline{vw}$ (Fig. 4c) reaches a maximum value at $s/t = -0.368$ approximately at $y^+ = 220$, at the same location of $-\overline{uv}$ (Fig. 5), with a value approximately twice the peak $-\overline{uv}$.

Ölçmen and Simpson (1995a) observed that $\left[(-\overline{uv})^2 + (-\overline{vw})^2\right]^{1/2}/\overline{v^2} = 1/S$ was nearly constant across the middle of the boundary layer for a number of different experimental 3D flow cases with $1/S \approx 0.6$. Around the vortex, profiles of $1/S$ do not have the same shape and much lower values of $1/S$ are observed ($1/S < 1/2$) than in the 3D flow away from the vortical structure, such as at $s/t = -0.667$ ($1/S \approx 1/2$). This parameter indicates that some of the v motion near the vortex is "inactive" (Bradshaw, 1967) and does not produce as strong Reynolds shearing stresses. Profiles of the Townsend ratio $A_1 = \left[(-\overline{uv})^2 + (-\overline{vw})^2\right]^{1/2}/(2TKE)$ also do not have the same shape and much lower values ($A_1 < 0.14$) are observed in regions around the vortex than in 2D flows ($A_1 \approx 0.15$) and at $s/t = -0.667$ ($A_1 \approx 0.14$). As shown in Fig. 5 the peak $A_1 = 0.18$ occurs under the upsweep side of the vortex, while the minimum A_1 is located to the side of the downwash side.

In the vicinity of the vortex core the triple products $\overline{u^2v}$, $\overline{v^3}$, and $\overline{vw^2}$ are larger than zero (Figs. 6 and 7), indicating that the intermittent, high "v" velocity fluctuations dominate the region. Additionally the largest values of $\overline{v^3}$ are at the downwash side of the mean vortical structure. These observations suggest that the instantaneous vortical structure intermittently rises as a whole away from the surface with a large instantaneous V velocity component. The negative values of $\overline{uv^2}$ also support the view that low momentum fluid is lifted away from the wall. Also, only large negative $\overline{v^2w}$ values are observed at this region. This observation indicates that seldom but strong negative "w" fluctuations occur in this region, which is believed to be due to the intermittently upward motion of the vortical structure, which exposes the region below the mean vortex core to higher negative instantaneous W velocity components.

3.3. Below the vortex core, nearer the wall, and including bimodal velocity region

The flow field in a region between the $\log_{10}(y/t) \approx -1.4$ and $\log_{10}(y/t) \approx -2.4$ below the core of the outer-layer vortex show double-peaked w fluctuating velocity histograms. It is believed that the high speed free-stream fluid carried closer to the wall beneath the vortex core during the occasional uplifting of the vortex results in large negative "w" velocity fluctuations in this region, and the occasional thinning of the vortical structures by stretching allow the upstream boundary layer flow mostly free of streamwise vortical motions to occupy the region. Within the duration of the occasional outer-layer vortex thinning the flow direction becomes closer to the tunnel coordinates direction with lower momentum than observed otherwise and result in positive "w" velocity fluctuations in the 22.4° coordinate system studied. These two separate flow events result in bimodal w histograms.

The flow within the bimodal w zone, whose location is shown in Figs. 3c, 5 and 7, reveals some information on its sources. For $s/t = -0.291$ and $\log_{10}(y/t) \approx -2.31$ ($y^+ \approx 27$), Fig. 8 shows joint probability distributions of the instantaneous flow angles for various instantaneous velocity ranges, q/U_{ref}. The free-stream flow that is redirected closer to the wall by the large vortex results in large velocity magnitude values and (Figs. 2a and 2b) and produces large $q/U_{\text{ref}} > 1$ in a single mode instantaneous flow angle distribution between $-50° < \arctan(w/u) < -25°$ with respect to the $x_{22.4}$ coordinates. At lower q/U_{ref} ranges, the flow becomes bimodal since the flow moving in a direction closer to the tunnel coordinates (close to the $x_{22.4}$ axis, and $-10° < \arctan(w/u) < 10°$) becomes more probable. For the lowest velocities, this latter mode is dominant. Thus we see that the bimodal w region is intermittently occupied by the high velocity spiraling vortical flow and flow that is about perpendicular to the plane. The maximum value of the $\overline{w^2}$ near the wall (Figs. 3c and 5) is much larger than the other normal stresses due to this aperiodic motion.

In this bimodal region where the negative W mean velocity is high, infrequent motions with high positive instantaneous W instantaneous velocity values result in high positive triple product values (Fig. 7). On the other hand high speed negative W instantaneous velocities result in negative values farther from the wing (Fig. 7), supporting the flow structure explained in the previous paragraph. Additionally, ejection motions ($u < 0, v > 0, w > 0$) result in negative $\overline{uw^2}$ values closer to the regions where $\overline{w^3}$ is positive (Fig. 7) and the sweep motions ($u > 0, v < 0, w < 0$) result in positive $\overline{uw^2}$ values closer to regions where $\overline{w^3}$ is negative. Near where the $\overline{w^3}$ triple product changes sign, $\overline{u^2v}$ reaches a positive maximum (Fig. 6a), indicating that seldom ejection motions occur around this region. In fact the $\overline{u^2v}$ is positive throughout the near-wall region.

Although very near the wall below $\log_{10}(y/t) \approx -2.5$ the $\overline{u^3}$ is positive and the $\overline{u^2v}$ is negative (Figs. 6a and 7) due to

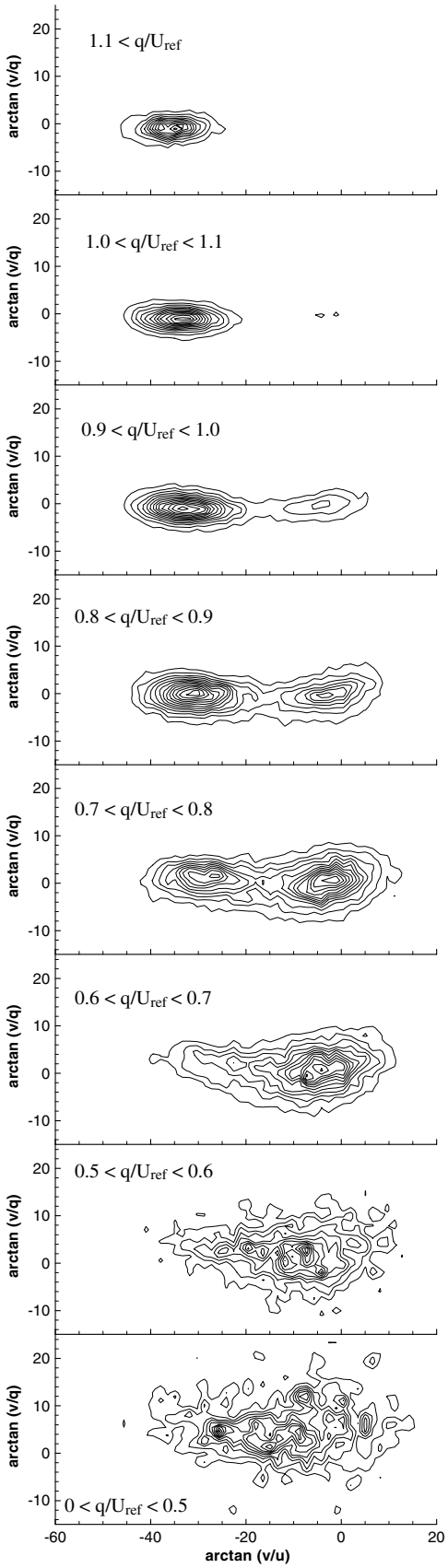

Fig. 8. Joint probability distributions of instantaneous flow angles for various instantaneous velocity ranges q/U_{ref} under horseshoe vortex, $s/t = -0.291$, $\log_{10}(y/t) = -2.31$.

sweep motions ($u > 0, v < 0$); above the $\overline{u^3} = 0$ line in Fig. 7 the $\overline{u^3}$ becomes negative while the $\overline{u^2 v}$ values become positive indicating that the ejection motions are important in that region. The $\overline{u^2 w}$ value becomes positive proceeding from $s/t = -0.368$ towards $s/t = -0.247$ and the maximum value increases, indicating that $\overline{u^2}$ momentum transport with a positive w transport velocity nearer the wing side of the vortex core. These observations on the components involving w fluctuating velocity component indicate that a clockwise intermittent vortical structure affects the flow field.

3.4. Near the wing/wall junction

In the wing/wall junction region ($-0.114 < s/t < -0.023$) high speed fluid with large negative V velocity components (Fig. 2b) is directed down the wing towards the wing/wall junction where it is redirected in the streamwise direction resulting in high U velocity components. A counter-clockwise comer vortex exists below $\log_{10}(y/t) \approx -1.6$. The U velocity gradients and spanwise vorticity near the wall become the largest in the plane of measurements (Fig. 2a). The wall-shear at location nearest the wing is 1.7 times that of the shear stress observed beneath the 3D TBL at the most outboard station. The W velocity gradients decrease as the wing is approached.

The $\overline{u^2}$ normal stress (Fig. 3a) reaches maxima at $y^+ \approx 15 (\log_{10}(y/t) \approx -2.75)$ with values about $\overline{u^2}/u_\tau^2 = 8.5$, similar to those observed in most outboard station in the measurement plane. However, the above $y^+ = 50$ the $\overline{u^2}$ fluctuations are suppressed to become less than the $\overline{v^2}$ fluctuations, with values as low as $(\overline{u^2}/u_\tau^2 = 0.5)$ or about the 1/6th of the values observed in the most outboard station, due to low turbulence free-stream flow being redirected into this region. The $\overline{w^2}$ stress peak $(\overline{w^2}/u_\tau^2 = 3.3)$ occurs closer to the wall at about $y^+ = 20$, as opposed to $y^+ = 125$ observed at the most outboard station with comparable values due to the high-speed downwash effect. The $\overline{v^2}$ stress not affected by this downwash show variations similar to the variations as at the most outboard station within the measurement plane. The shear stresses are much affected by the downwash and the near wing/wall proximity in this region. At station $s/t = -0.07$, the maximum $-\overline{uw}$ shear-stress value occurs at $y^+ \approx 15$, the $\overline{uv}$ stress becomes positive in the region $y^+ = 40$–300 and the $\overline{vw}$ stress is positive throughout the profile. A local maximum $\overline{uw}$ is observed at $s/t = -0.023$, at $y^+ \approx 5$ at station $s/t = -0.023$.

In this region the positive maximum $\overline{u^2 v}$, $\overline{u^2 w}$ and negative maximum $\overline{u^3}$ are located at about $\log_{10}(y/t) \approx -2.5$ at $s/t = -0.07$. The values decrease in all directions about this point and change sign as the wall is approached, indicating that the ejection motions ($U < 0, v > 0, w > 0$) are dominant away from the wall, and the sweep motions ($u > 0, v < 0$, $w < 0$) are the dominant motions near the wall. These observations also show that a clockwise intermittent vortical structure affects the flow field.

4. Flow, flow gradient, shear stress directions and eddy-viscosity ratio

The flow angle ($FA = \arctan(W/U)$) is defined with respect to the $x_{22.4}$ axis (Fig. 9a), and a positive flow angle shows a fluid motion towards the wing. While the positive maximum flow angle is observed at the boundary layer edge of the most outboard station at $s/t = -0.677$, the minimum value is located between the vortex core and the wall at $s/t = -0.24$ and $\log_{10}(y/t) \approx -2$. Large negative FA values below the vortex core indicates to the fact that the large negative W mean velocity values are present in this region. Near the wall/wing junction, positive flow angles are observed. The flow angles with opposite sign on each side of the separation zone indicate to a counter-clockwise vortical motion.

Flow-gradient angle ($FGA = \arctan((\partial W/\partial y)/(\partial U/\partial y))$) values show large variations between $-114°$ and $90°$ with respect to the $x_{22.4}$ line (Fig. 9b). A minimum value is obtained away from the vortex core, wing and the wall, and it is located below the vortex at $s/t = -0.35$, $\log_{10}(y/t) \approx -1.6$. The FGA shows large gradients between $\log_{10}(y/t) \approx -1.6$ and -2.2. Positive FGA values are located in the zone between the vortex and the wing. Sharp variations are also observed near the wing.

The shear-stress angle ($SSA = \arctan(\overline{vw}/\overline{uv})$) attain large positive values beneath the outer-layer vortex and large negative values near the wall in the $x_{22.4} - s$ plane of the measurements (Fig. 9c). Negative and positive values greater than $90°$ indicate a region where $-\overline{uv}$ shear stress is negative. A positive SSA shows a $-\overline{vw} > 0$ and negative SSA indicate a $-\overline{vw} < 0$. The plot shows that very near the wall at the separation location, the $-\overline{uv}$ shear stress is negative. In such a flow the SSA lags highly behind the FGA. Large variations by the FGA are not followed by the SSA.

The eddy-viscosity ratio $T = \mu_z/\mu_x = -\overline{vw}/(\partial W/\partial y)/-\overline{uv}/(\partial U/\partial y)$ is defined as the ratio of the eddy-viscosity terms defined along the s and the x directions. The most commonly used commercial codes using algebraic, one-equation and two-equation turbulence closure models use the approximation that the T assumes a value of unity. The eddy viscosity ratio, T relative to the local flow angle, which is coordinate system independent about the y-axis can be also written as

$$T = \frac{\tan(\mathrm{SSA} - \mathrm{FA})}{\tan(\mathrm{FGA} - \mathrm{FA})}$$

and the values are shown in Fig. 10. The figure shows that T is not a constant at any y for these data, and that T is about constant in the outer layer with values about $T \approx 0.4$–0.5. Whereever $\mathrm{FGA} = \mathrm{FA}$, the data show T approaching large negative or positive values. Fig. 10 also

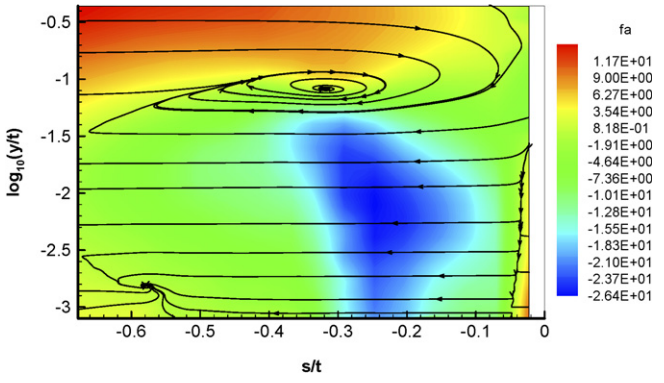

Fig. 9a. Flow angle (degrees) contours and secondary-flow streamlines.

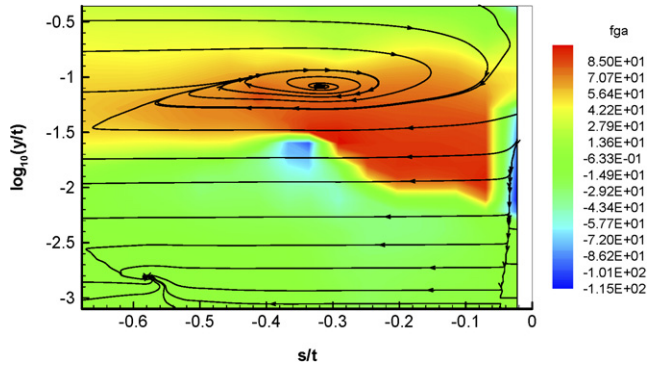

Fig. 9b. Flow-gradient angle (degrees) contours and secondary-flow streamlines.

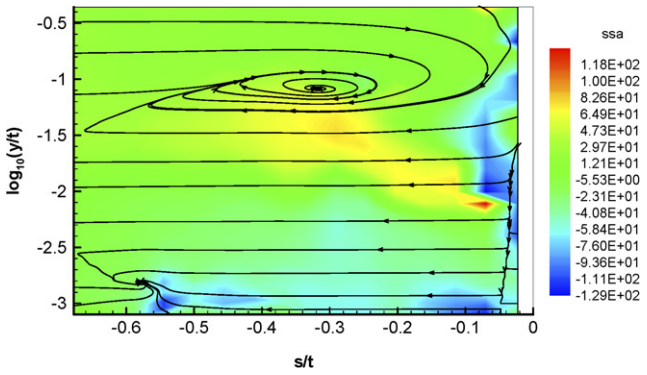

Fig. 9c. Shear-stress angle (degrees) contours and secondary-flow streamlines.

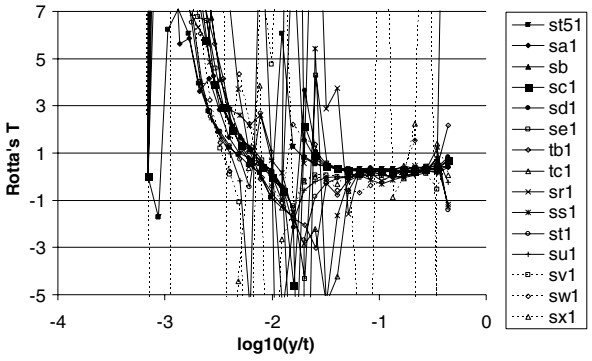

Fig. 10. Rotta's T eddy-viscosity ratio. Stations are listed starting with the most outboard station.

shows that, specifically below $\log_{10}(y/t) \approx -1.5$, the T values are far from being unity or a constant.

5. Conclusions

Laser-Doppler velocimetry data obtained at fifteen stations in a measurement plane perpendicular to the wing and the wall have been analyzed and some structural features of a wing–wall junction have been presented. The data show the presence of a complex flow field and four separate flow regions with different flow characteristics. A large outer-layer vortical flow occupies most of the flow field. Near the wall a three-dimensional separation region is observed away from the wing. A region in the vicinity of the wing–wall junction is observed where the flow is towards the wing, and a region below the outer-layer vortex where the lateral velocity component histograms show a bimodal nature.

Mean velocities and the higher order statistics show that spiraling motion of the outer-layer vortex redirects the high-momentum fluid to the vicinity of the wing–wall junction and also to beneath the outer-layer vortex resulting in both high mean velocity-magnitudes in these regions. Although the spiraling motions reenergize the low-momentum near wall flow beneath the large vortex, the negative pressure gradients produced by the wing shape along the s direction results in a three-dimensional separation region away from the wing. The flow in the vicinity of the wing/wall junction forms a vortical structure in the opposite sense of rotation to the outer-layer vortex. The flow field near the wall shows three distinct regions where the streamwise vorticity of the flow is in the opposite direction to that of the large outer-layer vortex. These regions are located around the 3D separation location, beneath the outer-layer vortex near the wall and in the vicinity of the wing/wall junction.

The third order statistics show that aperiodic stretching of the outer-layer vortical structure exposes the near wall flow to the approach boundary layer flow field, which flows in a direction closer to the tunnel coordinates, resulting in positive w fluctuations. The intermittent occasional lifting of the vortical structure allows the intermittent high-speed flow with negative W values to occupy the near wall region and results in negative w fluctuations. These two phenomena together result in bimodal w histograms with large $\overline{w^2}$ values obtained near the wall below the outer-layer vortex. Third order products also indicate that the intermittent vortical structures occur near the wall with an opposite sense to the mean vortical structures. Diffusion processes are highly altered by the outer-layer vortex effects on the inner layer flow. Large triple product magnitudes are observed surrounding the vortex core, below the vortex core, within the region between the vortex core and wing nearer the wall and near the wing/wall junction.

This complex flow field differs much from a three-dimensional turbulent boundary layer flow due to the presence of an aperiodic outer-layer vortex. The $\overline{u^2}$ normal stress local maxima occur right beneath the vortex core, near the wall beneath the vortex core and in the vicinity of the wing wall junction. The $\overline{v^2}$ maximum occurs below the vortex core and large $\overline{v^2}$ values occur around the vortex core due to intermittent lifting of the vortex as a whole. The $\overline{w^2}$ maximum occurs beneath the vortex core due to bimodal nature of the w fluctuations. The $\overline{w^2}$ is very large compared to $\overline{u^2}$ and $\overline{v^2}$ normal stresses, especially in the region between the vortex core and the wall. The turbulent kinetic energy of the flow increases to 5–6 times to that of the most outboard station values in regions where bimodal w fluctuations are observed. Both the $\overline{uv}$ and the $\overline{vw}$ stresses reach their maximum values on the uplifting side of the vortex core. The $\overline{uw}$ stress maxima are located near the wall below the vortex core closer to the wing and at the wing/wall junction.

In this flow field, the shear-stress angle severely lags behind the flow gradient angles. Where there are severe FGA variations, the SSA response in the outer layer is not followed in the inner regions. Indicating that most commonly used turbulence closure models assuming that the SSA and the FGA have the same magnitudes would not be able to calculate the flow field adequately. The linear eddy-viscosity models, such as the zero-equation models (e.g. Cebeci-Smith, Baldwin-Lomax), half-equation models (e.g. Johnson-King model), one-equation models (e.g. Spalart-Allmaras model), two-equation models (e.g. the standard k–ε and the k–ω models) assuming an isotropic eddy-viscosity are expected to result in unsatisfactory computational results (Launder and Sandham, 2002).

Acknowledgement

The authors are grateful for the support of the Office of Naval Research Grant N00014-94-1-0092, Dr. L. Patrick Purtell, Program Manager.

References

Ailinger, K., 1990. Measurements of surface shear stress under a three-dimensional turbulent boundary layer using oil-film laser interferometry. MSc. Thesis, Aerospace and Ocean Engineering Department, Virginia Tech, Virginia.

Apsley, D.D., Leschziner, M.A., 2001. Investigation of advanced turbulence models for the flow in a generic wing–body junction flow. Turbulence Combust. 67, 25–55.

Bonnin, J.C., Buchel, T., Rodi, W., 1996. ERCOFTAC workshop on data bases and testing of calculation methods for turbulent flows, ERCOFTAC Bulletin 28, March 1996.

Bradshaw, P., 1967. Inactive motion and pressure fluctuations in turbulent boundary layers. J. Fluid Mech. 30, 241–258.

Deng, G., Visonneau, M., 1999. Computation of a wing–body junction flow with a new Reynolds-stress transport model. In: Proc. 22nd Symp. Naval Hydor. National Academies Press, pp. 691–707.

Devenport, W.J., Simpson, R.L., 1987. Time-dependent structure in wing–body junction rows. In: Sixth Symposium on Turbulent Shear Flows. Toulouse, France, September 7–9, 1987Turbulent Shear Flows. Springer-Verlag, pp. 232–238, in selected papers volume.

Devenport, W.J., Simpson, R.L., 1990a. A time-dependent and time-averaged turbulence structure near the nose of a wing–body junction. J. Fluid Mech. 210, 23–55.

Devenport, W.J., Simpson, R.L., 1990b. An experimental investigation of the flow past an idealized wing–body junction: final report, VPI & SU report, VPI-AOE-172; DTIC: AD-A2296028XSP.

Devenport, W.J., Simpson, R.L., 1992. Flow past a wing–body junction—Experimental evaluation of turbulence models. AIAA J. 30 (4), 873–882.

Fleming, J., Simpson, R.L., Devenport, W.J., 1993. An experimental study of a turbulent wing–body junction and wake flow. Exp. Fluids 14, 366–378.

Holman, J.P., 2000. Experimental Methods for Engineers. McGraw-Hill Book Company.

Khan, M.J., Ahmed, A., Trosper, J.R., 1995. Dynamics of the juncture vortex. AIAA J. 33 (7), 1273–1279.

Kim, S., Walker, D.A., Simpson, R.L., 1991. Observation and measurement of flow structures in the stagnation region of a wing–body junction. Report VPI-E-91-20; submitted to DTIC.

Launder, Sandham, 2002. Closure Strategies for Turbulent and Transitional Flows. Cambridge University Press.

Lewis, D.J., Simpson, R.L., Diller, T., 1994. Time resolved surface heat flux measurements in the wing/body junction vortex. AIAA J. Thermophys. Heat Transfer 8, 656–663.

McMahon, H.M., Hubbart, J., Kubendran, L., 1982. Mean velocities and Reynolds stresses in a juncture flow, NASA Contractor report 3605.

McMahon, H.M., Merati, P., Yoo, K.M., 1987. Mean velocities and Reynolds stresses in the juncture flow and in the shear layer downstream of an appendage, Georgia Tech Report, GITAER 87-4, Atlanta, Georgia, 30332.

Ölçmen, M.S., 1990. An experimental study of a three-dimensional pressure-driven turbulent boundary layer, Ph.D. Dissertation, Virginia Tech, AOE Dept; Report-VPI-AOE-178. DTIC: ADA2294957XSP.

Ölçmen, M.S., Simpson, R.L., 1994. Influence of wing shapes on surface pressure fluctuations at wing–body junctions. AIAA J. 32 (1), 6–15.

Ölçmen, M.S., Simpson, R.L., 1995a. An experimental study of a three-dimensional pressure-driven turbulent boundary layer. J. Fluid Mech. 290, 225–262.

Ölçmen, M.S., Simpson, R.L., 1995b. A five-velocity-component laser-Doppler velocimeter for measurements of a three-dimensional turbulent boundary layer. Meas. Sci. Technol. 6, 702–716.

Ölçmen, M.S., Simpson, R.L., 1996a. Experimental evaluation of pressure–strain models in complex 3D turbulent flow near a wing/body junction, VPI & SU Report, VPI-AOE-228; DTIC-ADA307116. Available from: <http://stinet.dtic.mil/cgi-bin/GetTRDoc?AD=A307116&Location=U2&doc=GetTRDoc.pdf>.

Ölçmen, M.S., Simpson, R.L., 1996b, Experimental transport-rate budgets in complex 3D turbulent flow near a wing/body junction, AIAA-1996-2035. In: 27th AIAA Fluid Dynamics Conference, June 17–20, New Orleans, LA.

Ölçmen, M.S., Simpson, R.L., 1996c. Theoretical and experimental pressure–strain comparison in a pressure-driven three-dimensional turbulent boundary layer, AIAA-1996–2141. 1st AIAA Theoretical Fluid Mechanics Meeting, June 17–20, New Orleans, LA.

Ölçmen, M.S., Simpson, R.L., 1996d. Some structural features of a turbulent wing–body junction vortical flow, VPI & SU Report, VPI-AOE-238; DTIC- ADA321557. Available from: <http://stinet.dtic.mil/cgi-bin/GetTRDoc?AD=A321557&Location=U2&doc=GetTRDoc.pdf>.

Ölçmen, M.S., Simpson, R.L., 1996e. Higher order turbulence results for a three-dimensional pressure-driven turbulent boundary layer, VPI & SU Report, VPI-AOE-237; DTIC- ADA321516. Available from: <http://stinet.dtic.mil/cgi-bin/GetTRDoc?AD=A321516&Location=U2&doc=GetTRDoc.pdf>.

Ölçmen, M.S., Simpson, R.L., 1997. Some features of a turbulent wing–body junction vortical flow. AIAA-97-0651, 35th Aerospace Sciences Meeting and Exhibit, January 6–10, Reno, NV.

Ölçmen, M.S., Simpson, R.L., Kim, S., Ha, S.M., 1991. Some effects of appendage shape and a fence control device on appendage/hull junction flows, Virginia Tech, Report-VPI-AOE-183.

Parneix, S., Durbin, P.A., Behnia, M., 1998. Computation of 3d turbulent boundary layers using the v2-f model. Flow Turbul. Combust. 60, 19–46.

Rizzi, A., Vos, 1998. Toward establishing credibility in computational fluid dynamics simulations. AIAA J. 36 (5), 668–675.

Simpson, R.L., 1996. Aspects of turbulent boundary layer separation, Progress in Aerospace Sciences, November.

Simpson, R.L., 2001. Junction flows. Ann. Rev. Fluid Mech. 33, 415–443.

Sung, Chao-Ho, Yang, Cheng-1,1988. Validation of turbulent horseshoe vortex flows. In: 17th Symposium on Naval Hydrodynamics, 29 August–2 September, The Hague, Netherlands.

Wetzel, T.G., Simpson, R.L., Chesnakas, C.J., 1998. Measurement of three-dimensional crossflow separation. AIAA J. 36 (4), 557–564.